

Microporous Nitrogen-Doped Activated Biochars Derived from Corn: Use of Husk Waste and Urea for CO₂ Capture

Danilo Hisse,^{a,b} Isabela A. A. Bessa,^{id}^a Ludmila P. C. Silva,^b Aline F. M. da Silva,^{id}^a Joyce R. Araujo,^c Bráulio S. Archanjo,^c André V. H. Soares,^b Fabio B. Passos,^b José W. M. Carneiro,^a Thiago C. dos Santos^{id}^d and Célia M. Ronconi^{id}^{*,a}

^aDepartamento de Química Inorgânica, Universidade Federal Fluminense, Campus do Valonguinho, Outeiro São João Batista s/n, Centro, 24020-150 Niterói-RJ, Brazil

^bDepartamento de Engenharia Química e Petróleo, Universidade Federal Fluminense, Campus da Praia Vermelha, R. Passo da Pátria, 156, São Domingos, 24210-240 Niterói-RJ, Brazil

^cDivisão de Metrologia de Materiais, Instituto Nacional de Metrologia, Qualidade e Tecnologia (Inmetro), 25250-020 Duque de Caxias-RJ, Brazil

^dInstituto de Química, Universidade Federal do Rio de Janeiro. Av. Athos da Silveira Ramos 149, CT, Cidade Universitária, 21941-909 Rio de Janeiro-RJ, Brazil

The increase in anthropogenic activity over time has led to an exponential increase in greenhouse gas emissions, especially CO₂. Profitable technologies for CO₂ capture and separation are conspicuous, and porous biochars derived from biomass waste can be a useful solution. Herein, we produced activated nitrogen-doped biochars for CO₂ capture from corn husk waste, urea and K₂CO₃, named N-Bio-X (X = 600, 700, and 800 °C). N-Bio-X exhibited microporosity and different nitrogen contents and thus played an important role in the adsorption of CO₂. N-Bio-700 exhibited the highest CO₂ adsorption capacity, fastest adsorption kinetics and excellent stability after multiple adsorption-desorption cycles. N-Bio-600 showed excellent CO₂/N₂ selectivity, induced by nitrogen sites, particularly pyridinic and graphitic nitrogen. The cost-effectiveness of the raw material, coupled with its high adsorption capacity, rapid kinetics, and stable properties, provided highly promising N-doped biochars for practical implementation in CO₂ capture and separations in postcombustion processes.

Keywords: biomass, corn husk, urea, nitrogen-doped biochar, CO₂ capture and separation, postcombustion

Introduction

According to the Intergovernmental Panel on Climate Change (IPCC),¹ the burning of fossil fuels is responsible for approximately 70% of global CO₂ emissions. The environmental consequences of these emissions include rising global temperatures, ocean acidification and rising sea levels, all of which affect biodiversity and food security. To mitigate these impacts, the use of CO₂ capture technologies in industry and even in treating the atmosphere has been identified as a promising solution.¹ The European

Union has set a CO₂ capture target of 43 million tons by 2030. Therefore, a significant increase in CO₂ capture capacity is needed to reach these targets.^{2,3}

CO₂ capture and separation can be performed by chemical absorption using amine aqueous solutions,^{4,5} carbonate solutions,⁶ ionic liquids,⁷ adsorption on porous solid materials,^{8,9} membrane separations¹⁰ and cryogenic distillation.¹¹ Amine aqueous solutions for CO₂ absorption have been applied in coal-fired power generation and natural gas purification.¹² Although this method is very efficient, its high operating and maintenance costs, as well as the potential environmental impacts of its toxic byproducts arising from amine degradation, could restrict its extensive use for CO₂ capture in other applications.⁴ Therefore, significant effort has been made to develop environmentally friendly methods for low-cost CO₂ capture.

*e-mail: cmronconi@id.uff.br

Editor handled this article: Aldo José Gorgatti Zarbin (Guest)

Dedicated to the memory of Prof Oswaldo Luiz Alves for his contribution to the field of solid-state chemistry and for his passion for and dedication to science and teaching.



CO₂ adsorption has several advantages over other carbon capture technologies because it can be used in a variety of settings, such as power plants, industrial processes, and transportation, and it is easily integrated into existing structures. Moreover, these materials can be combined with other carbon capture technologies to improve their efficiency.

There are a variety of adsorbent materials for CO₂ capture, including carbon-based materials,^{9,13} ordered porous silicas,¹⁴⁻¹⁶ zeolites,^{17,18} metal-organic frameworks,¹⁹ and covalent-organic frameworks.⁸ These materials usually have high surface areas and pore volumes and tunable pore sizes. The selectivities and adsorption capacities of ordered porous silicas,¹⁴⁻¹⁶ zeolites,^{20,21} metal-organic frameworks,^{19,22,23} and covalent-organic frameworks toward CO₂ can be improved by surface or pore chemical functionalization with amino groups.

Carbon-based materials, particularly biochars, are promising adsorbents for CO₂ capture because they can be obtained from biomass waste, which reduces the costs of production and is easily scalable.²⁴⁻²⁸ Currently, agricultural residues, including eucalyptus bark,²⁹ banana and grapefruit peel,³⁰ rice husk³¹ and coconut,^{32,33} peanut,^{34,35} and macadamia nutshells,³⁶ have been used as feedstocks to produce porous carbon-based materials for the adsorption of organic pollutants, heavy metals and CO₂.^{37,38} Biochars are thermally stable and highly microporous, have high CO₂ adsorption capacities at low pressures, exhibit fast CO₂ adsorption/desorption kinetics and are therefore good candidates for CO₂ capture and separation in postcombustion processes.^{39,40} Additionally, the affinities and selectivities of these materials for CO₂ can be improved by the introduction of nitrogen atoms into their frameworks through copyrolysis with nitrogen-containing compounds such as melamine,⁴¹ ethylenediamine,⁴² sodium amide,⁴³ and urea.⁴⁴ The nitrogen species are more basic than the carbon atoms and they improve the CO₂ adsorption capacities at low pressures and thus increase the CO₂ selectivity of the gas mixture. The adsorption capacity can also be improved by the addition of KOH to the biomass during pyrolysis to increase the surface area and pore volume of the resulting material.⁴⁵ At temperatures higher than 600 °C, KOH reacts with the carbon framework to remove carbon and create pores.⁴⁰ However, alkaline KOH is a corrosive and hazardous chemical, and other activating reagents, such as K₂CO₃, have been proposed to create porosity.⁴⁶

In this work, N-doped activated biochars for CO₂ capture (N-Bio-X, X = 600, 700 and 800 °C) were prepared from corn husk as a feedstock, urea as a nitrogen source and K₂CO₃ as an activating agent. As the second largest agricultural area in the world, corn produces a large amount

of corn husk waste and can be used as a biomass source to produce biochars.⁴⁷ This practice can promote waste reduction by developing sustainable and efficient materials, thereby safeguarding our natural resources.⁴⁸ However, to our knowledge, few studies have explored this biomass as a feedstock for biochar preparation for use as an adsorbent for CO₂ capture. Because urea is an inexpensive chemical, it has become an interesting nitrogen-containing compound with which to dope biochar from corn husks. Therefore, we investigated the effects of activation temperature on the surface area, pore volume, pore size and nitrogen percentage of N-Bio-X and correlated these properties with the CO₂ adsorption capacity, thermodynamics, and selectivity. Kinetic and cyclic adsorption-desorption studies were also carried out to understand the behavior of the synthesized biochars under CO₂ flow.

Experimental

Materials

The following reactants and solvents were used: potassium carbonate (K₂CO₃, P.A., Sigma-Aldrich, St. Louis, USA), urea (NH₂)₂CO, 99.5%, Sigma-Aldrich, St. Louis, USA), ethanol (EtOH, 95%, Isofar, Duque de Caxias, Brazil) and hydrochloric acid (HCl, 37%, Isofar, Duque de Caxias, Brazil). Corn husks were purchased from a local market.

Preparation of biochar from corn husk biomass (Bio-500)

The corn husks were washed with water, dried at 100 °C for 2 h and ground in a conventional blender until a homogeneous powder was formed. Then, the powder (535 g) was heated at 500 °C (10 °C min⁻¹) under a static air atmosphere for 2 h. The obtained biochar was named Bio-500 (10 g) and used as a precursor to obtain nitrogen-doped biochars. Elemental analysis (CHN) of the Bio-500 samples revealed the following: C, 73.20%; H, 3.16%; and N, 1.71%.

Preparation of N-doped and activated carbons (N-Bio-X, X = 600, 700 and 800 °C)

The preparation of the biochars is schematically represented in Figure 1.

In a porcelain mortar, 1.0 g of the Bio-500 precursor, 1.0 g of urea and 1.5 g of K₂CO₃ with a mass ratio of 1:1:1.5 were ground to obtain a homogeneous mixture, which was subsequently added to a 100 mL beaker containing 80 mL of EtOH. The mixture was heated to 80 °C and stirred

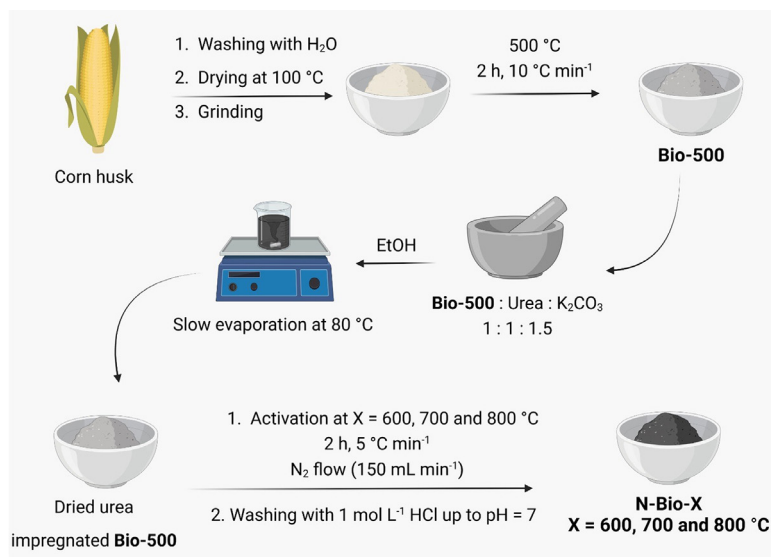


Figure 1. Representation of the procedure employed for the preparation of the biochars.

magnetically until solvent evaporation. The black solid was dried at 90 °C in a drying oven. The resulting solid was introduced in a vertical furnace on a glass wool surface and heated at 600, 700 or 800 °C under a N₂ atmosphere (150 mL min⁻¹) at a heating rate of 5 °C min⁻¹ for 2 h. The resulting products were washed with 1 mol L⁻¹ HCl to remove the remaining unreacted K₂CO₃ and then with distilled water up to neutral pH. The solids were dried at 110 °C overnight to form nitrogen-doped biochars, which were named N-Bio-X (X = 600, 700 and 800 °C), yielding 0.33 g (N-Bio-600), 0.27 g (N-Bio-700) and 0.20 g (N-Bio-800) of each material. Elemental analyses (CHNs) were performed for N-Bio-600: C, 62.01%; H, 2.91%; N, 3.58%; N-Bio-700: C, 57.12%; H, 3.43%; N, 2.12%; N-Bio-800: C, 56.74%; H, 4.05%; and N, 0.74%.

Characterization techniques

The CHN contents were determined with a PerkinElmer (Shelton, USA) CHN 240 C Elemental Analyzer (IQ-USP). Powder X-ray diffraction (PDRX) patterns were acquired on a Miniflex Rigaku II (Tokyo, Japan) diffractometer (Cu K α radiation = 1.5418 Å) with a 2 θ range of 10–60°. Raman spectra were collected on a Witec Alpha 300 spectrometer (Ulm, Germany) using an excitation laser at $\lambda = 532$ nm and a 50 \times lens glass. X-ray photoelectron spectroscopy (XPS) was performed with a Thermo Scientific Escalab 250Xi (Waltham, USA) system with monochromated Al K α radiation (1486.6 eV). The survey spectra were recorded using 0.2 eV steps and a 100 eV analyzer pass energy. The high-resolution N 1s binding energies were measured with a 25 eV analyzer pass energy with 0.2 eV steps. Deconvolutions of the signals

centered at 400.1 eV (N 1s) were carried out with CasaXPS software.⁴⁹ Nitrogen adsorption/desorption isotherms were measured on a Micromeritics ASAP 2020 (Norcross, USA) system at –196 °C. For these measurements, the samples were pretreated at 180 °C under vacuum for 24 h. The Brunauer-Emmett-Teller (BET) equation and the Horvath-Kawazoe (HK) method were used to determine the specific surface areas and cumulative pore volumes, respectively. Transmission electron microscopy (TEM) images were obtained with a probe-corrected FEI Titan 80-300 (Hillsboro, USA) transmission electron microscope (80 kV). The images were acquired in scanning TEM (STEM) mode using a high-angle annular dark-field (HAADF) detector. The samples were prepared by dispersing 1.0 mg of the biochars in isopropyl alcohol (3 mL) in an ultrasonic bath for 10 min. Then, one drop of the dispersion was placed on a lacey carbon copper grid (300 mesh) and dried at room temperature.

CO₂ adsorption experiments

CO₂ isotherms were measured in the low-pressure regime (0–1 bar) at three different temperatures, 25, 50 and 70 °C, with a Micromeritics ASAP 2020 (Norcross, USA) system. The equilibrium parameters were obtained using three adsorption mathematical models, the Langmuir, Freundlich and Toth equations, with the datafit function of the free software Scilab.⁵⁰ The best model was selected based on the normalized standard deviations. The adsorption enthalpy was calculated from the Clausius-Clapeyron equation. The same temperature and pressure conditions used to obtain CO₂ isotherms were used to obtain N₂ isotherms and determine the CO₂/N₂ selectivities (IAST_{CO₂/N₂}).

The selectivity $I_{AST_{CO_2/N_2}}$ was calculated using the ideal adsorption solution theory (IAST) derived from Henry's law and the Gibbs isotherm equations.⁵¹

Kinetic CO₂ uptake adsorption experiments

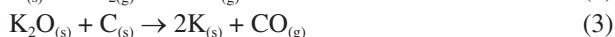
The kinetic isotherms for CO₂ uptake were obtained on a Shimadzu DTG-60/60-H TG (Japan) apparatus based on the procedure reported by Yang *et al.*⁵² The samples (7.0 mg) were placed in alumina crucibles and pretreated at 120 °C under a N₂ flow of 50 mL min⁻¹ for 1 h or until the mass stabilized. The temperature was cooled to 30 °C, and CO₂ was added to the sample (50 mL min⁻¹), whereas a N₂ flow (50 mL min⁻¹) was passed through the balance. The CO₂ uptake adsorption was measured until no mass variation was detected (equilibrium), and then the CO₂ flow was switched off to allow CO₂ desorption until the initial mass was reached. The desorption time was held the same for each cycle. This procedure was repeated seven times.

Results and Discussion

Syntheses of the nitrogen-doped biochars: Bio-500 and N-Bio-X (X = 600, 700 and 800 °C)

Biochar Bio-500 was obtained by heating ground corn husk waste at 500 °C under a static air atmosphere for 2 h. The percentage of nitrogen in Bio-500, determined by elemental analysis, was 1.71%. Corn husks usually contain proteins and lignin-containing nitrogen compounds, which can be incorporated into biochar as nitrogen atoms during thermal decomposition.⁵³⁻⁵⁵ We added more nitrogen atoms to Bio-500 by using urea as the nitrogen source and K₂CO₃ to activate the material at different calcination temperatures, resulting in nitrogen-doped biochars N-Bio-X (X = 600, 700 and 800 °C).

At high temperatures, K₂CO₃ decomposed into CO₂ and K₂O, etched the carbon atoms in the lattice of Bio-500 and produced microporous structures based on the reactions shown in equations 1 to 3. At temperatures higher than 700 °C and in the presence of K₂CO₃, the pore volume and/or size increase.^{40,56}



The N-doping process occurs via thermal decomposition of urea and is a complex process depending on the heating temperature.^{57,58} Briefly, at temperatures above 133 °C, urea decomposes into ammonia, biuret, triuret, and isocyanic

acid.⁵⁸ The latter compound can further decompose into cyanuric acid, which sublimates at temperatures above 300 °C. The percentages of nitrogen atoms incorporated into the biochars, as determined by elemental analyses, were 3.58, 2.12, and 0.74% for the N-Bio-600, N-Bio-700, and N-Bio-800 samples, respectively. The percentage of nitrogen atoms decreased as the activation temperature increased, which may be attributed to thermal reactions of the incorporated nitrogen atoms.

Wang and co-workers^{36,59-61} reported the effect of the activator amount on the development of the material porosity. Increasing the activator ratio in the feedstock resulted in higher values of specific surface area and pore volume. Nonetheless, Tanaka and co-workers⁶² observed a pore widening feedstock effect employing higher quantities of K₂CO₃ as an activating agent as a result of increasing meso- and macropore volumes. Aiming to produce adsorbent solids for postcombustion applications, we fixed a low feedstock:activating agent ratio (1:1) to prioritize the obtainment of microporous solids to capture CO₂ in the low-pressure regime.

Characterizations

Characterization of the biochars via XPS (survey) revealed C 1s (285.1 eV), N 1s (400.1 eV) and O 1s (533.1 eV) signals for all the samples (Figure 2a). To investigate the nature of the nitrogen atoms incorporated into the samples, as shown in Figure 2b, high-resolution XPS spectra were obtained (Figures 2c-2f). Deconvolution of the signal centered at 400.1 eV (N 1s) using the software CasaXPS resulted in three signals. The signals at 398.6 and 400.1 eV were assigned to pyridinic and pyrrolic nitrogen, respectively.^{13,63-65} The signal at 402.5 eV was in the range of graphitic nitrogen (401.1-402.7 eV) and pyridinic nitrogen oxide (402.6 eV).^{49,66} Considering the anoxic environment present during the preparation of N-doped materials under a N₂ atmosphere, graphitic N was more likely to form than pyridinic N-oxide was. The percentages calculated from the areas of the C 1s, N 1s and O 1s signals in the survey spectra, as well as the percentage of each type of nitrogen-containing functional group found in the high-resolution spectra, are shown in Table 1. The nitrogen percentages obtained from elemental analyses are also listed in Table 1 for comparison.

The percentages of nitrogen in the biochars calculated from the XPS data were similar to those obtained from the elemental analyses (Table 1). Most importantly, both nitrogen determinations (XPS and elemental analysis) showed similar tendencies involving decreases in the nitrogen percentage as the activation temperature increased.

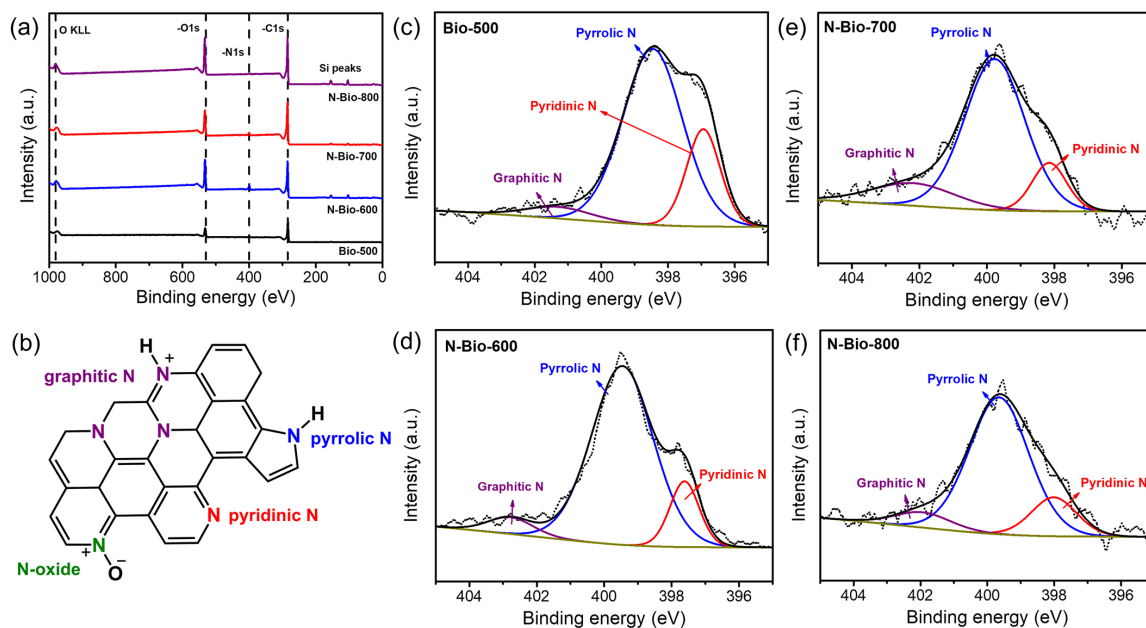


Figure 2. (a) XPS survey spectra of Bio-500, N-Bio-600, N-Bio-700 and N-Bio-800. The Si peaks are contaminations from glass wool used in the activation process. (b) Possible N-containing functional groups in the biochars. High-resolution N 1s spectra of (c) Bio-500, (d) N-Bio-600, (e) N-Bio-700 and (f) N-Bio-800.

Table 1. Percentages of C, O and N atoms in the biochars determined by X-ray photoelectron spectroscopy (XPS)

Biochar	Percentage / %						
	C	O	N	N (EA) ^a	Pyrrolic-N	Graphitic-N	Pyridinic-N
Bio-500	83.77	14.22	2.01	1.71	1.45	0.10	0.45
N-Bio-600	75.38	19.60	5.02	3.58	4.04	0.28	0.71
N-Bio-700	80.93	16.47	2.60	2.12	1.87	0.38	0.34
N-Bio-800	78.55	20.91	0.54	0.74	0.41	0.04	0.09

^aPercentage of nitrogen atoms determined from elemental analysis.

The Raman spectra of the biochars are displayed in Figure 3a. There were two bands, one ca. 1350 cm^{-1} and the other ca. 1580 cm^{-1} , related to the D-band and G-band, respectively. The G signal is due to the E_{2g} phonon, and the D band is due to the breathing modes of sp^2 rings and requires defects for activation.^{67,68} The I_D/I_G ratio indicates the degree of structural defects in the biochar materials. The I_D/I_G values for Bio-500 and N-Bio-600 were determined to be 0.80 and 0.96, respectively, suggesting a significant increase in the proportion of structural defects in the latter biochar. These defects may include edges, grain boundaries, vacancies, inserted atoms, and changes in carbon hybridization (from sp^2 to sp^3).⁴⁸ The I_D/I_G ratios for N-Bio-700 and N-Bio-800 were 1.00 and 1.02, respectively. By comparing the I_D/I_G ratios of the N-doped biochars (N-Bio-600, N-Bio-700, and N-Bio-800) with that of the precursor Bio-500, we observed a gradual increase in the number of structural defects in the N-doped samples (Table S1, Supplementary Information (SI) section). The

enhanced defect formation in N-Bio-600 compared to that in Bio-500 may be attributed to the incorporation of nitrogen atoms into the carbon structure of the precursor and the activation process. However, the smoother increases in defects observed for N-Bio-600, N-Bio-700, and N-Bio-800 were most likely influenced by the activation temperature rather than by nitrogen insertion into the carbon structures.

PDXR patterns revealed low crystallinities for all the biochars, as expected (Figure 3b). The two broad peaks at 2θ ca. 24° (002) and 43° (100) were attributed to the interlayer distances and 2D in-plane graphitic structures, respectively.^{69,70}

N_2 physisorption isotherms and cumulative pore volume curves were recorded to investigate the porosity of the biochars (Figures 4a-4b and Table 2). The specific surface areas (S_{BET}) obtained by the BET method were 355 $\text{m}^2 \text{g}^{-1}$ for Bio-500, 1095 $\text{m}^2 \text{g}^{-1}$ for N-Bio-600, 1521 $\text{m}^2 \text{g}^{-1}$ for N-Bio-700, and 1944 $\text{m}^2 \text{g}^{-1}$ for N-Bio-800. According to the IUPAC classification, all of the biochars exhibited

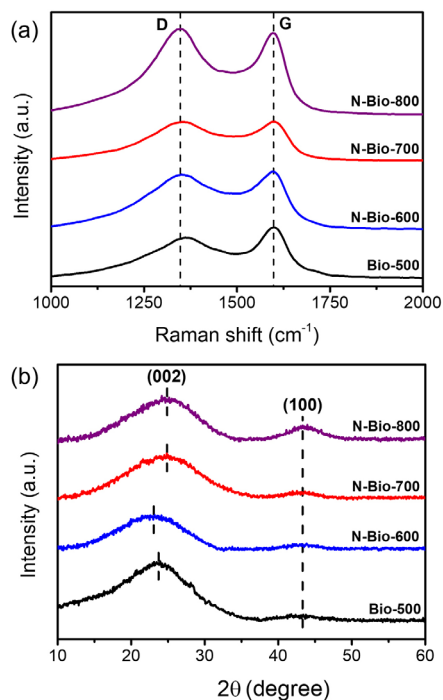


Figure 3. (a) Raman spectra and (b) PXRD patterns of Bio-500, N-Bio-600, N-Bio-700 and N-Bio-800.

combinations of type I and IV isotherms.⁷¹ Type I isotherms are characteristic of microporous materials, in which solid-gas interactions occur predominantly at low pressures ($p/p_0 < 0.01$). With increasing activation temperature, the saturation points of the N₂ isotherm curves shifted to higher pressures, indicating enlarged pore sizes. The cumulative pore volume distributions, which were calculated using the Horvath-Kawazoe method,⁷² provided insight into the volumes of pores smaller than 1 nm, between 1 and 2 nm, and larger than 2 nm (Table 2). Furthermore, we plotted the volumes of micropores smaller than 1 nm and larger than 1 nm for the biochars (Figure 4c). The results showed that the total volume of micropores smaller than 1 nm was twice the volume of pores larger than 1 nm (including micropores and mesopores). Considering the volumes for micropores smaller than 1 nm, as the activation temperature increased, the micropore volume increased linearly, but the slopes of the curves decreased as the temperature increased from N-Bio-700 to N-Bio-800 (Figure 4c). For pore volumes larger than 1 nm, which included micropores and mesopores, the opposite effect occurred, with increasing slopes observed for N-Bio-700 to N-Bio-800. Our findings were consistent with results described in the literature.⁷³⁻⁷⁵ For example, McKee⁷³ investigated the catalytic effects of various alkali metal carbonate salts on the gasification of carbon-based materials and observed a maximum carbon gasification rate when using K₂CO₃ at 800 °C, which

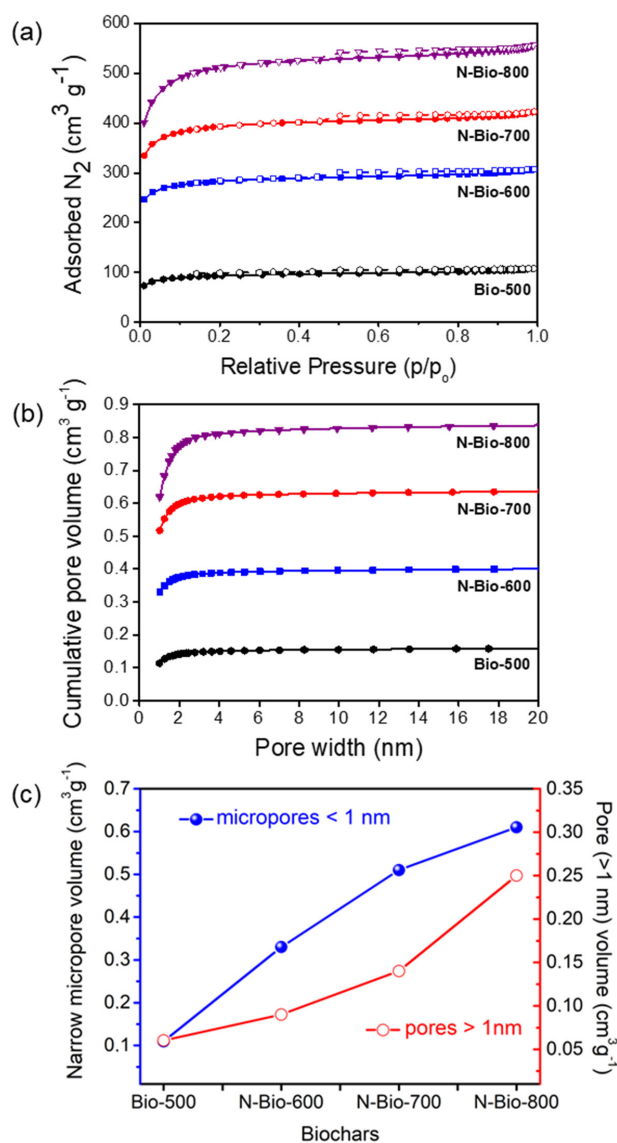


Figure 4. (a) N₂ isotherms and (b) cumulative pore volume of Bio-500, N-Bio-600, N-Bio-700 and N-Bio-800. (c) Correlations between the volumes of micropores smaller than 1 nm and pores larger than 1 nm for the biochars.

increased the volume contribution from pores larger than 2 nm. Similarly, Kim *et al.*⁷⁵ reported an increase in the mesopore volume of biochar produced from coffee grains activated with K₂CO₃ at temperatures above 800 °C.

STEM images of the activated N-doped biochars revealed sponge-like structures with pore sizes on the nanometer scale, whereas the precursor Bio-500 showed a less porous structure, indicating that K₂CO₃ efficiently activated the materials (Figure 5). The images also revealed that as the activation temperature increased, the structures of the biochars became more leafed, porous, curved and wrinkled, thereby increasing the porosities of the samples, which was consistent with the BET surface areas (Table 2).

Table 2. Textural parameters, percentages of nitrogen atoms from elemental analyses, and CO₂ adsorption capacities of Bio-500, N-Bio-600, N-Bio-700 and N-Bio-800 at 1 bar

Biochar	S _{BET} / (m ² g ⁻¹)	V _{total} / (cm ³ g ⁻¹)	V _{narrow} / (cm ³ g ⁻¹)	V _{micro} / (cm ³ g ⁻¹)	V _{meso} / (cm ³ g ⁻¹)	N / %	CO ₂ / (mmol g ⁻¹)
Bio-500	355	0.17	0.11	0.03	0.03	2.01	1.66
N-Bio-600	1095	0.41	0.33	0.05	0.04	5.02	3.38
N-Bio-700	1521	0.65	0.51	0.08	0.06	2.60	4.23
N-Bio-800	1944	0.86	0.61	0.16	0.09	0.54	3.70

S_{BET}: specific surface area calculated by the BET method; V_{total}: total micropore and mesopore volume; V_{narrow}: micropore volume for sizes < 1 nm; V_{micro}: micropore volume for sizes between 1 and 2 nm; V_{meso}: mesopore volume for sizes > 2 nm; N: percentages of nitrogen atoms from XPS analyses; CO₂: adsorption capacities at 1 bar and 25 °C. XPS: X-ray photoelectron spectroscopy.

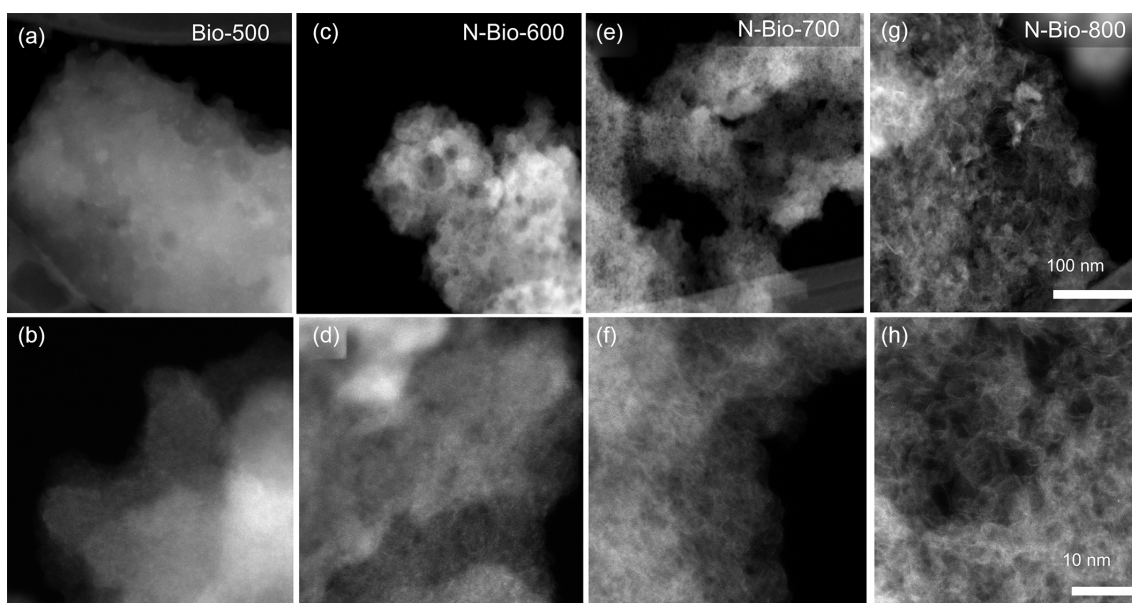


Figure 5. STEM images of (a) and (b) Bio-500, (c) and (d) N-Bio-600, (e) and (f) N-Bio-700 and (g) and (h) N-Bio-800 obtained at different magnifications.

CO₂ adsorption isotherms

The CO₂ adsorption isotherms indicating the amount of CO₂ adsorbed by the biochars in mmol of CO₂ per gram of

biochar were obtained at 25 °C and at low pressures, and the results are shown in Figure 6a and Table 2. All of the N-doped activated biochars displayed higher CO₂ adsorption capacities than did the nonactivated biochar Bio-500, revealing that

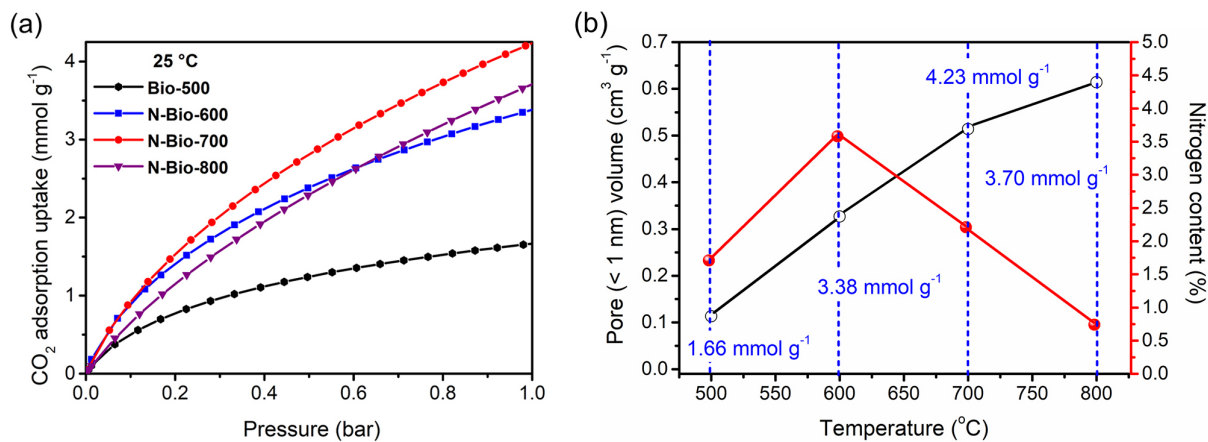


Figure 6. (a) CO₂ adsorption isotherms of Bio-500, N-Bio-600, N-Bio-700 and N-Bio-800 at 25 °C. (b) A plot relating the CO₂ adsorption capacities at 1 bar, the narrow micropore volumes (< 1 nm) and the nitrogen contents obtained from the XPS analyses to the temperatures used for activation of the N-doped biochars.

the addition of urea and the activation processes involving K_2CO_3 at different temperatures increased the CO_2 adsorption capacities of the solids. This difference was related to the combination of several properties of the N-doped activated biochars, such as greater surface areas and higher micropore volumes than those of Bio-500, particularly for pores with sizes smaller than 1 nm. Additionally, the amount of nitrogen inserted in the carbon structures of the N-doped biochars may also have important effects on the CO_2 adsorption capacities and selectivities (Table 3).

N-Bio-800, with a BET surface area of $1944 \text{ m}^2 \text{ g}^{-1}$, exhibited a lower CO_2 adsorption capacity (3.70 mmol g^{-1}) at 1 bar than did N-Bio-700 (4.23 mmol g^{-1}), with a BET surface area of $1521 \text{ m}^2 \text{ g}^{-1}$. It is well known from the literature that under low pressures, microporous materials are efficient gas adsorbents because the small distances between opposite walls produce effective adsorption force fields.⁸⁰ We plotted a graph relating the narrow micropore volumes (< 1 nm) and nitrogen percentages to the activation temperatures of the N-doped biochars (Figure 6b). When comparing biochars Bio-500, N-Bio-600 and N-Bio-700, increases in micropore volume (< 1 nm) were followed by increased CO_2 adsorption ($1.66\text{--}4.73 \text{ mmol g}^{-1}$). However, as previously mentioned, N-Bio-800 had a greater micropore volume and lower CO_2 adsorption capacity than did N-Bio-700, indicating that other properties, such as the percentage of nitrogen, should be considered to explain this result. When the percentage of nitrogen increased to an activation temperature of $600 \text{ }^\circ\text{C}$, the value decreased, e.g., the nitrogen percentage for N-Bio-800 was 0.54%, while

that for N-Bio-700 was 2.60% (Table 2). The insertion of nitrogen atoms into the carbon structure can improve the CO_2 adsorption capacity because nitrogen is more electronegative than carbon.¹³ Nitrogen atoms produce localized charge regions, improving the interactions between CO_2 and the adsorbent.¹³ The results obtained in the present work indicate a synergistic effect between the micropore volume (< 1 nm) and the percentage of nitrogen inserted in the N-doped biochars, which is dependent on the activation temperature, determining the CO_2 adsorption capacity. Therefore, the N-biochar activated at $700 \text{ }^\circ\text{C}$ had a high nitrogen percentage and high volume for micropores smaller than 1 nm, which led to the highest CO_2 adsorption capacity among the synthesized materials.

Equilibrium isotherm models

Figure 7 shows the experimental CO_2 adsorption isotherms measured at 25, 50 and $75 \text{ }^\circ\text{C}$ for Bio-500 and N-Bio-X (X = 600, 700 and $800 \text{ }^\circ\text{C}$), respectively, and their respective fits to the Langmuir, Freundlich and Toth models.^{81,82} The parameters obtained from each fitted equilibrium model are displayed in Table S2 (SI section).

In the Langmuir model, the adsorbate remains static on the adsorbent surface, and the interactions between them present a homogeneous energy distribution.⁸³ The Langmuir equation is written as follows:

$$q_e = \frac{q_{mL} K_L P}{1 + K_L P} \quad (4)$$

Table 3. Comparison between CO_2 selectivities and other properties of the N-doped biochars prepared in this work and those of N-doped biochars described in the literature

Sample	Biomass	Nitrogen source; nitrogen amount / wt.%	Selectivity at $25 \text{ }^\circ\text{C}$	$S_{\text{BET}} / (\text{m}^2 \text{ g}^{-1})$	CO_2 adsorption capacity at $25 \text{ }^\circ\text{C}$ (1 bar) / (mmol g^{-1})	Reference
			Y_{CO_2}/Y_{N_2} (15:85)			
N-Bio-600	corn husk	$(NH_2)_2CO$; 5.02 ^a	53.74	1095	3.38	this work
N-Bio-700	corn husk	$(NH_2)_2CO$; 2.60 ^a	19.12	1521	4.23	this work
N-Bio-800	corn husk	$(NH_2)_2CO$; 0.54 ^a	6.96	1944	3.70	this work
BC600	banana peel	$(NH_2)_2CO$; 3.15 ^a	17.45	3098	3.59	Li <i>et al.</i> ³⁰
GG600	grapefruit peel	$(NH_2)_2CO$; 3.37 ^a	10.59	2996	3.05	Li <i>et al.</i> ³⁰
SG-CN(2)	sugarcane bagasse	melamine; 3.4 ^b	–	1111	3.34	Adio <i>et al.</i> ⁴¹
CAC-5	rice husk	chitosan; 8.61 ^a	15.3	1496	3.68	He <i>et al.</i> ⁷⁶
CAC-6	rice husk	chitosan; 4.79 ^a	20.4	1638	ca. 2.80	He <i>et al.</i> ⁷⁶
CP800	corn cob powder	none; 1.57 ^a	ca. 13	827	ca. 3.4	Li <i>et al.</i> ⁷⁷
CPU800	corn cob powder	$(NH_2)_2CO$; 3.12 ^a	ca. 24	1016	ca. 3.8	Li <i>et al.</i> ⁷⁷
CKC-900-4	corn kernel	none	19	1726	3.63	Wu <i>et al.</i> ⁷⁸
RHC-PC-2	rice husk	none	37.80	1343	3.40	Gan <i>et al.</i> ⁷⁹

^aN content determined by XPS (X-ray photoelectron spectroscopy) analysis; ^bN content determined by EDX. S_{BET} : specific surface area calculated by the BET method.

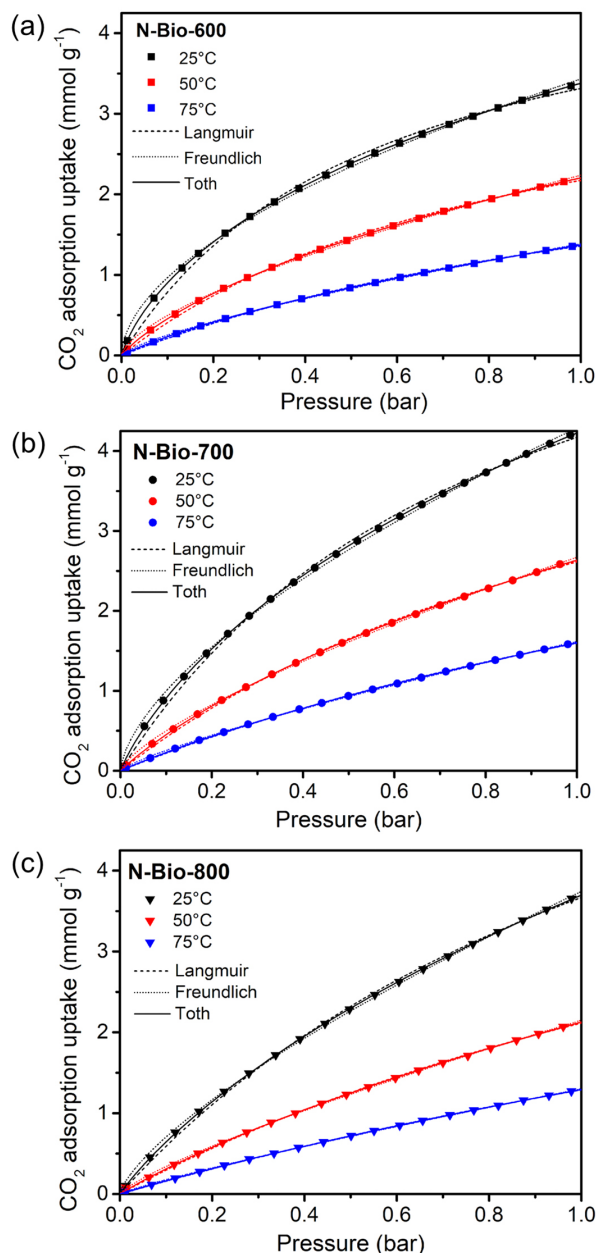


Figure 7. Experimental CO₂ adsorption isotherms and curve fits with the Langmuir, Freundlich and Toth equations for (a) N-Bio-600, (b) N-Bio-700 and (c) N-Bio-800 measured at 25, 50 and 75 °C.

where q is the amount of CO₂ adsorbed (mmol g⁻¹) at pressure P , q_{m_L} (mmol g⁻¹) is the maximum monolayer adsorption capacity and K_L (bar⁻¹) is the Langmuir constant related to the free energy of adsorption. The Freundlich equation was given by He *et al.*:⁷⁶

$$q_e = K_F P^{\frac{1}{n_F}} \tag{5}$$

where K_F (mmol g⁻¹ bar^{-n_F}) and n_F are parameters that refer to the adsorption capacity and adsorption intensity between the adsorbent and adsorbate, respectively.

The Toth isotherm is usually applied to describe heterogeneous adsorption systems and is expressed as follows:⁸⁴

$$q_e = \frac{q_{m_T} K_T P}{\left(1 + (K_T P)^{n_T}\right)^{\frac{1}{n_T}}} \tag{6}$$

where P is the pressure (bar), q_{m_T} (mmol g⁻¹) is the saturation loading, K_T (bar⁻¹) is the equilibrium constant and n_T characterizes the heterogeneity of the system.

The goodness of fit between the experimental equilibrium data and the models was determined from the normalized standard deviation (Δq):

$$\Delta q = 100 \times \sqrt{\frac{\sum \left[\frac{(q_{e(\text{exp})} - q_{e(\text{mod})})}{q_{e(\text{exp})}} \right]^2}{n - 1}} \tag{7}$$

where n is the number of experimental points and the subscripts “exp” and “mod” refer to the experimental adsorption data and the adsorption data calculated by the models, respectively.⁸⁴

From the values of Δq (Table S2, SI section), we conclude that the Toth isotherm model gave the best fit to the CO₂ adsorption equilibrium data for the N-doped biochars. Notably, for the CO₂ isotherms of N-Bio-600, N-Bio-700 and N-Bio-800, the values were less than 1 (Table S2), revealing that the biochar surfaces were energetically heterogeneous and that the CO₂ was absorbed to form multilayers.⁸⁵ The equilibrium constant (K_T) decreased as the adsorption temperature increased (Table S2), indicating that high adsorption temperatures disfavored solid-gas interactions. Moreover, the K_T values obtained at the same adsorption temperature for N-Bio-600, N-Bio-700 and N-Bio-800 decreased as the N-doped biochar activation temperature increased, suggesting that the strength of the solid-gas interactions decreased in the order N-Bio-600 > N-Bio-700 > N-Bio-800. This difference in solid-gas interaction strength could be associated with the greater percentage of nitrogen in the N-Bio-600 sample than in the N-Bio-700 and N-Bio-800 samples. As we previously mentioned, the nitrogen atoms inserted into biochars could improve the interactions between CO₂ molecules and adsorbents through the formation of localized charge regions. Most likely, based on the values (< 1) determined by the Toth model, these nitrogen atoms might be heterogeneously distributed across the surface.

The N₂ isotherms measured at 25 °C for N-Bio-X (X = 600, 700 and 800 °C) were also fitted with the

Langmuir, Freundlich and Toth models (Figure S1 and Table S3, SI section). The Toth model again provided the best fit. In contrast to CO₂ adsorption, the N₂ adsorption capacity was independent of the nitrogen percentage present in the N-doped biochars. Moreover, the N₂ adsorption capacity increased as the specific surface area increased.

Isosteric heats of CO₂ adsorption

The Clausius-Clapeyron equation (equation 8) was used to calculate the isosteric heats of CO₂ adsorption on the N-doped biochars, with the adsorption isotherms measured at 25, 50 and 75 °C (Figure S2). Due to the goodness of fit between the Toth model and the experimental equilibrium data, we used such curves to apply the Clausius-Clapeyron equation.

$$Q_{st} = -R \left[\frac{\partial \ln(P)}{\partial (1/T)} \right]_n \quad (8)$$

where Q_{st} (kJ mol⁻¹) is the isosteric heat for the amount adsorbed n (mmol g⁻¹), P (bar) is the pressure, T (K) is the adsorption temperature and R (8.314 10⁻³ kJ mol K⁻¹) is the universal gas constant. The slope of the $\ln(P)$ versus $1/T$ plot was $\frac{\partial \ln(P)}{\partial (1/T)}$ (Figure S3). The negative values of the isosteric heats (Q_{st}) observed in Figure 8 confirmed the exothermic nature of the process and explained the decreased CO₂ adsorption capacities of the biochars with increases in the temperatures of the isotherms, as observed in Figure 7. The isosteric heat decreased for all the N-doped biochars as the CO₂ coverage increased from 0.01 to 2.00 mmol g⁻¹ (Figure 8). Most likely, the CO₂ molecules preferentially adsorbed on the most energetic sites on the surfaces of the biochars, i.e., the nitrogen sites, and then, as these sites were occupied, adsorption occurred on the less energetic sites.⁸⁶ Moreover, the greater surface heterogeneity of N-Bio-600 than of the other samples was indicated by the most prominent variation in its isosteric heat as the CO₂ coverage increased. Considering the uptake of 0.01 mmol g⁻¹ CO₂ (Figure 8), the calculated isosteric heat became less negative as the activation temperature of the N-doped biochar increased, e.g., -34.15 kJ mol⁻¹ for N-Bio-600, -30.50 kJ mol⁻¹ for N-Bio-700 and -27.43 kJ mol⁻¹ for N-Bio-800. These results were consistent with those obtained from the Toth model, which confirmed that the N-Bio-600 sample, which had the highest nitrogen percentage and was the most energetic and heterogeneous surface, formed the strongest interactions with CO₂. In addition, the type of nitrogen incorporated in biochar, e.g., pyridinic, graphitic

or pyrrolic, is important for solid-gas interactions.¹³ All nitrogen species may interact with CO₂; however, the interaction with pyridinic nitrogen might be stronger than that with pyrrolic nitrogen because the lone pair on the nitrogen atom of the pyridinic ring is available to interact with the acidic CO₂ molecule. The graphitic nitrogen types, particularly those containing nitrogen in the *meta* position of the ring, can strongly interact with CO₂ due to the high polarization caused by nitrogen substitution. Indeed, N-Bio-600, which presented the most negative isosteric heat (Q_{st}), was the solid containing the highest percentage of pyridinic and graphitic nitrogen atoms (0.99%) in comparison with N-Bio-700 (0.72%) and N-Bio-800 (0.13%) (see Table 1).

The relatively low values are commonly associated with the physisorption process. According to the literature, the optimal range is typically -30 to -50 kJ mol⁻¹. Materials with higher isosteric heats of adsorption require more energy to undo the formed interactions and promote desorption, which can have negative economic implications.⁸⁷

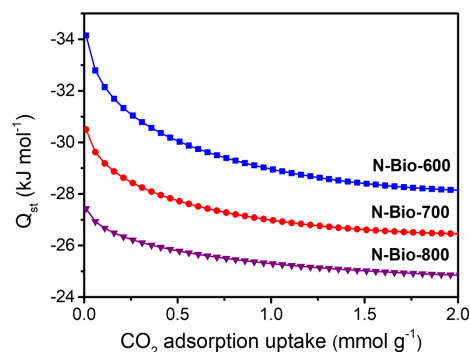


Figure 8. Isosteric heats for CO₂ adsorption onto N-Bio-600, N-Bio-700 and N-Bio-800.

Selectivity studies (CO₂/N₂)

Postcombustion is used in thermoelectric power plants and in the fertilizer industry. The combustion of coal or natural gas in the presence of air releases a gas flow at a pressure of 1 bar, which contains a low concentration of CO₂ (approximately 15%), a high content of N₂ (approximately 78%) and low percentages of other gases such as H₂O, O₂, CO, NO_x and SO_x.¹³ Therefore, the separation between CO₂ and N₂ must occur via adsorbents with high CO₂ selectivities at low pressures. The recovery of adsorbents containing CO₂ is conducted by heating and/or under vacuum.¹³ Therefore, it is necessary to investigate the selectivities of new adsorbent materials for CO₂ and N₂.

Figure 9a shows the CO₂ and N₂ adsorption branch isotherms measured at 25 °C. All of the N-doped biochars

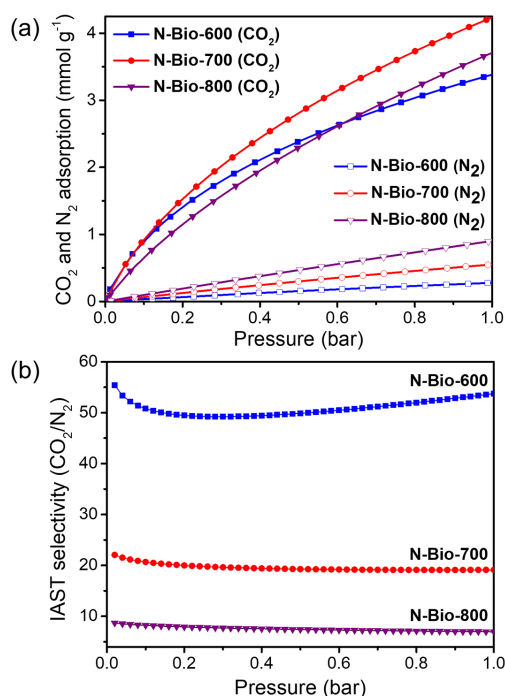


Figure 9. (a) CO_2 and N_2 adsorption isotherms measured at 25 °C (the open symbols refer to N_2 , and the closed symbols refer to CO_2) and (b) the IAST CO_2 selectivities of N-Bio-600, N-Bio-700 and N-Bio-800.

adsorbed much greater amounts of CO_2 than N_2 . Because CO_2 has a smaller kinetic diameter, a higher quadrupole moment (CO_2 , $13.4 \times 10^{-40} \text{ C m}^2$; N_2 , $4.7 \times 10^{-40} \text{ C m}^2$) and a higher polarizability (CO_2 , $29.0 \times 10^{-25} \text{ cm}^3$; N_2 , $17.4 \times 10^{-25} \text{ cm}^3$) than N_2 , more CO_2 is expected to be adsorbed on N-doped biochars.⁷¹

A comparison of the N_2 adsorption capacities of the N-Bio-X materials ($X = 600, 700$ and $800 \text{ }^\circ\text{C}$) revealed that the increase in adsorption strength was proportional to the increase in activation temperature. This result is ultimately related to the increased specific surface areas and pore volumes of N-Bio-X (Table 2). In contrast, the CO_2 adsorption behavior did not depend only on the increased surface areas of the biochars, as previously discussed.

The selectivity for a binary mixture of CO_2 and N_2 at 25 °C can be calculated with the ideal adsorbed solution theory (IAST) from the single-component adsorption isotherms for CO_2 and N_2 .⁷² For the selectivity calculation, the ratio in the nonadsorbed phase was 85/15, which is the typical composition of the gases exhausted in the postcombustion process for a binary composition.^{73,74} The selectivity can be calculated by solving equations 9 and 10 for the variable.⁸² The calculation was conducted using the functions integrate and solved in the free software Scilab.⁵⁰ The results are usually represented in the literature with equation 11.

$$\int_0^{y_{\text{CO}_2}} \frac{n_{\text{CO}_2}(P_{\text{CO}_2})}{P_{\text{CO}_2}} dP_{\text{CO}_2} = \int_0^{y_{\text{N}_2}} \frac{n_{\text{N}_2}(P_{\text{N}_2})}{P_{\text{N}_2}} dP_{\text{N}_2} \quad (9)$$

$$x_{\text{N}_2} + x_{\text{CO}_2} = 1 \quad (10)$$

$$\text{IAST}_{\text{CO}_2/\text{N}_2} = \frac{x_{\text{CO}_2}}{x_{\text{N}_2}} \frac{y_{\text{N}_2}}{y_{\text{CO}_2}} \quad (11)$$

where P is the pressure, P_{CO_2} and P_{N_2} are the partial pressures of CO_2 and N_2 , x_{CO_2} and x_{N_2} are the molar fractions of CO_2 and N_2 in the adsorbed phase, y_{CO_2} and y_{N_2} are the molar fractions of CO_2 and N_2 in the nonadsorbed phase, and n_{CO_2} and n_{N_2} can be represented by adsorption equilibrium models; for the reasons already presented, we decided to use the Toth model. Figure 9b shows the IAST selectivities.

The N-doped biochars studied in this work exhibited $x_{\text{CO}_2}/x_{\text{N}_2} > 1$, considering $y_{\text{N}_2}/y_{\text{CO}_2} = 85/15$. Therefore, all the N-doped biochars were more selective for CO_2 than for N_2 , and N-Bio-600 was the most selective. Although N-Bio-700 adsorbs more CO_2 than does N-Bio-600, the selectivity of the former was 2.8 times lower than that of the latter.

Table 3 shows a comparison of the CO_2 selectivities, nitrogen percentages, BET surface areas and CO_2 adsorption capacities at 1 bar for the N-doped biochars prepared in this work with those of N-doped biochars obtained from different biomasses and described in the literature.

Table 3 shows that N-Bio-600 was the most selective toward CO_2 , but N-Bio-700 adsorbed more CO_2 . As previously discussed, increasing the activation temperature of the biochar resulted in increases in the specific surface area and total pore volume, which were beneficial for N_2 adsorption. However, a high activation temperature enlarged the pore sizes (Table 3) and reduced the nitrogen percentage on the surfaces of the biochars. Consequently, the selectivity toward CO_2 decreased because the larger pores also adsorbed N_2 , which presented a larger kinetic diameter. Additionally, the smaller the nitrogen percentage in the sample was, the weaker the interaction with CO_2 was, which decreased the selectivity.

Kinetic studies

Figure 10a shows the results of the CO_2 adsorption kinetic studies. The kinetic behaviors of the N-Bio-X ($X = 600, 700$ and $800 \text{ }^\circ\text{C}$) samples were similar to those of Bio-500. High adsorption rates were observed in the first 45 s. After one minute of the experiment, the adsorption rate decreased until kinetic equilibrium was reached. After three minutes, no significant changes in CO_2 adsorption were observed. There are reports of much

longer times (ca. 60 min) required to reach CO₂ adsorption kinetic equilibrium for N-carbon-based materials.^{75,88} All the materials prepared in this work exhibited similar adsorption rates, i.e., 0.45, 0.38 and 0.46 mmol g⁻¹ min⁻¹ for N-Bio-600, N-Bio-700 and N-Bio-800, respectively, demonstrating fast adsorption and diffusion of CO₂ in the pores. This result agrees with the low isosteric heat values (Figure 8) typical of physical adsorption driven by van der Waals forces, which does not involve activation energy, resulting in a fast adsorption process.⁸⁹ Adsorbents with a combination of micro- and mesopores show good mass transfer.⁹⁰ The N-doped biochars prepared in this work presented comparable mesopore volume percentages: 9.42% (N-Bio-600), 8.42% (N-Bio-700) and 10.0% (N-Bio-800). Because the interactions between CO₂ and mesopores are energetically less favorable than those between CO₂ and micropores, the presence of mesopores will facilitate gas access to micropores. Therefore, a higher mesopore volume is expected to result in faster adsorption. As the N-doped biochars prepared in this work exhibited similar mesopore volume percentages, the adsorption rates were also similar. Adsorbents with fast adsorption rates are interesting for practical carbon capture applications due to the high exhaust gas flow rates observed in industry.

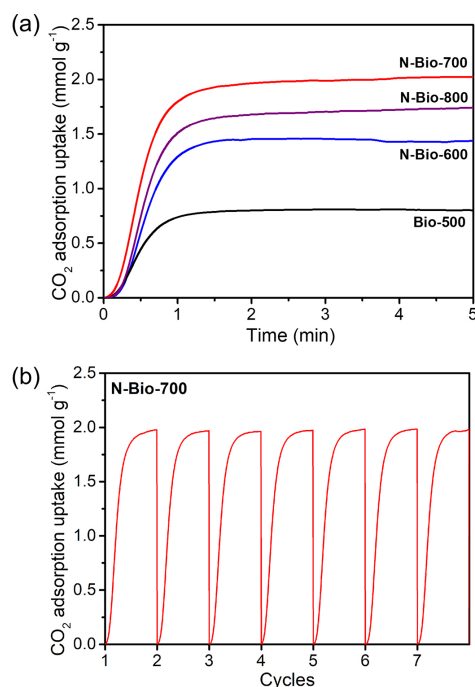


Figure 10. (a) CO₂ adsorption kinetic curves for Bio-500, N-Bio-600, N-Bio-700 and N-Bio-800 and (b) CO₂ adsorption and desorption cycles for N-Bio-700 measured at 30 °C (the desorption time was the same for each cycle).

Considering that more CO₂ was adsorbed by N-Bio-700 than by the other synthesized biochars,

we investigated cyclic CO₂ adsorption to evaluate its reusability (Figure 10b). The results revealed that N-Bio-700 remained stable for up to seven CO₂ adsorption/desorption cycles. Desorption was induced by flowing nitrogen at room temperature, possibly due to the low isosteric heat of N-Bio-700. This characteristic is important since, in chemical absorption technologies, the heat required for the regeneration of amine aqueous solutions makes the process very costly.⁹¹

Conclusions

In conclusion, microporous N-doped activated biochars derived from corn husks, K₂CO₃ as the activating agent and urea as the doping compound showed promise for CO₂ capture in postcombustion processes. At 25 °C and 1 bar, CO₂ adsorption studies showed that the adsorption capacities increased in the order Bio-500 (1.66 mmol g⁻¹) < N-Bio-600 (3.38 mmol g⁻¹) < N-Bio-800 (3.70 mmol g⁻¹) < N-Bio-700 (4.23 mmol g⁻¹). N-Bio-700 exhibited the highest performance due to the synergistic combination of the volume derived from micropores smaller than 1 nm (0.51 cm³ g⁻¹) and the percentage of nitrogen atoms (2.60%) on the surface. The Toth model describes the CO₂ and N₂ isotherms for all the N-doped biochars, and from the fitting parameters, the isosteric adsorption heat and the selectivity were calculated for a binary mixture of N₂/CO₂ (85/15). The isosteric heats ranged from -25 to -34 kJ mol⁻¹, confirming that physisorption was the predominant adsorption mode for CO₂ capture. Moreover, N-Bio-600 was the most energetic and heterogeneous surface because it had the highest percentage of nitrogen (5.02%). This material also demonstrated the highest selectivity toward CO₂ under the studied conditions. Kinetic studies revealed that adsorption equilibrium was reached in less than 3 min with the biochars. Regeneration studies demonstrated that N-Bio-700 maintained stability over multiple adsorption and desorption cycles. Therefore, both N-Bio-600 and N-Bio-700 are very promising biochars for CO₂ capture at low pressures.

Supplementary Information

Supplementary information (Raman wavenumber and I_D/I_G ratio for Bio-500 and N-Bio-X; fitted parameters of the experimental CO₂ isotherms of N-Bio-X; experimental and curve fittings of N₂ isotherms; fitted parameters of the experimental N₂ isotherms of N-Bio-X; CO₂ adsorption isotherms of N-Bio-X; and ln(P) versus 1/T (K⁻¹) plots used to calculate the isosteric heat of adsorption (Q_{st}) for N-Bio-X) is available free of charge at <http://jbcs.sbq.org.br> as PDF file.

Acknowledgments

This work was supported by the Brazilian agencies Conselho Nacional de Desenvolvimento Científico e Tecnológico (CNPq), Coordenação de Aperfeiçoamento de Pessoal de Nível Superior (CAPES) and Fundação Carlos Chagas Filho de Amparo à Pesquisa do Estado do Rio de Janeiro (FAPERJ). We are grateful to Molecular Spectroscopy and Material Characterization Multiuser Laboratories from Fluminense Federal University.

Author Contributions

Danilo Hisse was responsible for experimental work up, data curation, writing original draft; Isabela A. A. Bessa for experimental work up, data curation, writing original draft; Ludmila de Paula C. Silva for experimental work up; Aline F. M. da Silva for data curation, writing-review and editing; Joyce R. Araujo for data curation; Bráulio S. Archanjo for data curation; André V. H. Soares for data curation, formal analysis; Fabio B. Passos for funding acquisition, project administration; José Walkimar de M. Carneiro for writing-review and editing; Thiago C. dos Santos for formal analysis, investigation, writing-review and editing; Célia M. Ronconi for conceptualization, funding acquisition, project administration, writing-review and editing.

References

- Pachauri, R. K.; Allen, M. R.; Barros, V. R.; Broome, J.; Cramer, W.; Christ, R.; Church, J. A.; Clarke, L.; Dahe, Q.; Dasgupta, P.; Dubash, N. K.; Edenhofer, O.; Elgizouli, I.; Field, C. B.; Forster, P.; Friedlingstein, P.; Fuglestvedt, J.; Gomez-Echeverri, L.; Hallegatte, S.; Hegerl, G.; Howden, M.; Jiang, K.; Cisneros, B. J.; Kattsov, V.; Lee, H.; Mach, K. J.; Marotzke, J.; Mastrandrea, M. D.; Meyer, L.; Minx, J.; Mulugetta, Y.; O'Brien, K.; Oppenheimer, M.; Pereira, J. J.; Pichs-Madruga, R.; Plattner, G.-K.; Pörtner, H.-O.; Power, S. B.; Preston, B.; Ravindranath, N. H.; Reisinger, A.; Riahi, K.; Rusticucci, M.; Scholes, R.; Seyboth, K.; Sokona, Y.; Stavins, R.; Stocker, T. F.; Tschakert, P.; van Vuuren, D.; van Ypersele, J.-P.; *Climate Change 2014: Mitigation of Climate Change*, IPCC Fifth Assessment Report, Cambridge University Press, 2015. [Crossref]
- Global CCS Institute, *Global Status of CCS Report: 2020*, <https://www.globalccsinstitute.com/resources/publications-reports-research/global-status-of-ccs-report-2020/>, accessed in February 2024.
- Chagas, J. A. O.; Marciniak, A. A.; Mota, C. J. A.; *J. Braz. Chem. Soc.* **2022**, *33*, 801. [Crossref]
- dos Santos, T. C.; Lage, M. R.; da Silva, A. F. M.; Fernandes, T. S.; Carneiro, J. W. M.; Ronconi, C. M.; *J. CO₂ Util.* **2022**, *61*, 102054. [Crossref]
- Furtado, I. O.; dos Santos, T. C.; Vasconcelos, L. F.; Costa, L. T.; Fiorot, R. G.; Ronconi, C. M.; Carneiro, J. W. M.; *Chem. Eng. J.* **2021**, *408*, 128002. [Crossref]
- de Vasconcelos, S. F.; Carneiro, L. O.; Brito, R. P.; Brito, K. D.; *J. Braz. Chem. Soc.* **2023**, *34*, 441. [Crossref]
- Aquino, A. S.; Bernard, F. L.; Vieira, M. O.; Borges, J. V.; Rojas, M. F.; Vecchia, F. D.; Ligabue, R. A.; Seferin, M.; Menezes, S.; Einloft, S.; *J. Braz. Chem. Soc.* **2014**, *25*, 2251. [Crossref]
- Freitas, S. K. S.; Oliveira, F. L.; dos Santos, T. C.; Hisse, D.; Merlini, C.; Ronconi, C. M.; Esteves, P. M.; *Chem. Eur. J.* **2021**, *27*, 2342. [Crossref]
- dos Santos, T. C.; Ronconi, C. M.; *J. CO₂ Util.* **2017**, *20*, 292. [Crossref]
- Wang, X.; Song, C.; *Front. Energy Res.* **2020**, *8*, 265. [Crossref]
- Quang, D. V.; Milani, D.; Abu Zahra, M.; *Int. J. Greenhouse Gas Control* **2023**, *124*, 103862. [Crossref]
- Ribeiro, M. G.; Hisse, D.; Prado, M. L.; dos Santos, T. C.; Ronconi, C. M.; *Rev. Virtual Quim.* **2022**, *14*, 517. [Crossref]
- dos Santos, T. C.; Mancera, R. C.; Rocha, M. V. J.; da Silva, A. F. M.; Furtado, I. O.; Barreto, J.; Stavale, F.; Archanjo, B. S.; De Carneiro, J. W. M.; Costa, L. T.; Ronconi, C. M.; *J. CO₂ Util.* **2021**, *48*, 101517. [Crossref]
- dos Santos, T. C.; Bourrelly, S.; Llewellyn, P. L.; Carneiro, J. W. D. M.; Ronconi, C. M.; *Phys. Chem. Chem. Phys.* **2015**, *17*, 11095. [Crossref]
- Mello, M. R.; Phanon, D.; Silveira, G. Q.; Llewellyn, P. L.; Ronconi, C. M.; *Microporous Mesoporous Mater.* **2011**, *143*, 174. [Crossref]
- dos Santos, T. C.; Ronconi, C. M.; *Rev. Virtual Quim.* **2014**, *6*, 112. [Crossref]
- Babu, P. E.; Tejes, P. K. S.; Naik, B. K.; *Carbon Capture Sci. Technol.* **2023**, *7*, 100103. [Crossref]
- Najafi, A. M.; Soltanali, S.; Khorashe, F.; Ghassabzadeh, H.; *Chemosphere* **2023**, *324*, 138275. [Crossref]
- Dinda, S.; *Mater. Today Commun.* **2023**, *35*, 105927. [Crossref]
- Salih, H. A.; Alkhatib, I. I. I.; Zahra, M. A.; Vega, L. F.; *J. CO₂ Util.* **2023**, *68*, 102383. [Crossref]
- Short, G. N.; Burentugs, E.; Proaño, L.; Moon, H. J.; Rim, G.; Nezam, I.; Korde, A.; Nair, S.; Jones, C. W.; *JACS Au* **2023**, *3*, 62. [Crossref]
- Huang, Z.; Ying, L.; Gong, F.; Lu, J.; Wang, W.; Ding, J.; Yan, J.; *J. Environ. Chem. Eng.* **2023**, *11*, 109739. [Crossref]
- Ahn, H.; Xu, R.; Kim, S.; Lee, J. W.; Kang, Y. T.; *J. Environ. Chem. Eng.* **2023**, *11*, 109723. [Crossref]
- Zhang, X.; Cao, L.; Xiang, W.; Xu, Y.; Gao, B.; *Sep. Purif. Technol.* **2022**, *295*, 121295. [Crossref]
- Bamdad, H.; Hawboldt, K.; Macquarrie, S.; *Energy Fuels* **2018**, *32*, 11742. [Crossref]
- Chatterjee, R.; Sajjadi, B.; Chen, W. Y.; Mattern, D. L.; Egiebor, N. O.; Hammer, N.; Raman, V.; *Energy Fuels* **2019**, *33*, 2366. [Crossref]

27. Wu, B.; Song, X.; Zheng, D.; Tan, Q.; Yao, Y.; Liu, F. Q.; *ACS Appl. Mater. Interfaces* **2023**, *15*, 20325. [Crossref]
28. Li, D.; Chen, W.; Wu, J.; Jia, C. Q.; Jiang, X.; *J. Mater. Chem. A* **2020**, *8*, 24977. [Crossref]
29. Kortunov, P. V.; Siskin, M.; Paccagnini, M.; Thomann, H.; *Energy Fuels* **2016**, *30*, 1223. [Crossref]
30. Li, W.; Tu, W.; Cheng, J.; Yang, F.; Wang, X.; Li, L.; Shang, D.; Zhou, X.; Yu, C.; Yuan, A.; Pan, J.; *Sep. Purif. Technol.* **2022**, *282*, 120001. [Crossref]
31. Li, D.; Ma, T.; Zhang, R.; Tian, Y.; Qiao, Y.; *Fuel* **2015**, *139*, 68. [Crossref]
32. Yue, L.; Xia, Q.; Wang, L.; Wang, L.; DaCosta, H.; Yang, J.; Hu, X.; *J. Colloid Interface Sci.* **2018**, *511*, 259. [Crossref]
33. Liang, W.; Luo, Z.; Zhou, D.; Liu, Z.; Wei, X.; Cai, W.; *Chem. Eng. J.* **2023**, *461*, 141980. [Crossref]
34. Luo, Z.; Peng, X.; Liang, W.; Zhou, D.; Dang, C.; Cai, W.; *Bioresour. Technol.* **2023**, *388*, 129762. [Crossref]
35. Peng, X.; Luo, Z.; Xie, H.; Liang, W.; Luo, J.; Dang, C.; Wang, A.; Hu, L.; Yu, X.; Cai, W.; *Appl. Surf. Sci.* **2022**, *606*, 154859. [Crossref]
36. Bai, J.; Huang, J.; Yu, Q.; Demir, M.; Kilic, M.; Altay, B. N.; Hu, X.; Wang, L.; *Fuel Process Technol.* **2023**, *249*, 107854. [Crossref]
37. Khan, M. H.; Akash, N. M.; Akter, S.; Rukh, M.; Nzediegwu, C.; Islam, M. S.; *J. Environ. Manage.* **2023**, *338*, 117825. [Crossref]
38. Hanif, A.; Aziz, M. A.; Helal, A.; Abdelnaby, M. M.; Khan, A.; Theravalappil, R.; Khan, M. Y.; *ACS Omega* **2023**, *8*, 36228. [Crossref]
39. Ghanbarpour Mamaghani, Z.; Hawboldt, K. A.; MacQuarrie, S.; *J. Environ. Chem. Eng.* **2023**, *11*, 109643. [Crossref]
40. Zaker, A.; ben Hammouda, S.; Sun, J.; Wang, X.; Li, X.; Chen, Z.; *J. Environ. Chem. Eng.* **2023**, *11*, 109741. [Crossref]
41. Adio, S. O.; Ganiyu, S. A.; Usman, M.; Abdulazeez, I.; Alhooshani, K.; *Chem. Eng. J.* **2020**, *382*, 122964. [Crossref]
42. Ma, X.; Su, C.; Liu, B.; Wu, Q.; Zhou, K.; Zeng, Z.; Li, L.; *Sep. Purif. Technol.* **2021**, *259*, 118065. [Crossref]
43. Rao, L.; Liu, S.; Wang, L.; Ma, C.; Wu, J.; An, L.; Hu, X.; *Chem. Eng. J.* **2019**, *359*, 428. [Crossref]
44. Luo, J.; Liu, B.; Shi, R.; Guo, Y.; Feng, Q.; Liu, Z.; Li, L.; Norinaga, K.; *Microporous Mesoporous Mater.* **2021**, *327*, 111404. [Crossref]
45. Chun, S.-E.; Whitacre, J. F.; *Microporous Mesoporous Mater.* **2017**, *251*, 34. [Crossref]
46. Hayashi, J.; Yamamoto, N.; Horikawa, T.; Muroyama, K.; Gomes, V. G.; *J. Colloid Interface Sci.* **2005**, *281*, 437. [Crossref]
47. Ratna, A. S.; Ghosh, A.; Mukhopadhyay, S.; *J. Cleaner Prod.* **2022**, *371*, 133563. [Crossref]
48. Fattahi, M.; Taban, E.; Soltani, P.; Berardi, U.; Khavanin, A.; Zaroushani, V.; *J. Building Engineering* **2023**, *77*, 107468. [Crossref]
49. Ayiania, M.; Smith, M.; Hensley, A. J. R.; Scudiero, L.; McEwen, J. S.; Garcia-Perez, M.; *Carbon* **2020**, *162*, 528. [Crossref]
50. *Scilab*, 6.10; French Institute for Research in Computer Science and Control, Vélizy-Villacoublay, France, 1984.
51. Cessford, N. F.; Seaton, N. A.; Düren, T.; *Ind. Eng. Chem. Res.* **2012**, *51*, 4911. [Crossref]
52. Yang, J.; Yue, L.; Hu, X.; Wang, L.; Zhao, Y.; Lin, Y.; Sun, Y.; DaCosta, H.; Guo, L.; *Energy Fuels* **2017**, *31*, 4287. [Crossref]
53. Yang, X.; Han, F.; Xu, C.; Jiang, S.; Huang, L.; Liu, L.; Xia, Z.; *Ind. Crops Prod.* **2017**, *109*, 241. [Crossref]
54. Del Río, J. C.; Rencoret, J.; Gutiérrez, A.; Kim, H.; Ralph, J.; *J. Agric. Food Chem.* **2018**, *66*, 4402. [Crossref]
55. Yeasmin, M. S.; Mondal, M. I. H.; *Int. J. Biol. Macromol.* **2015**, *80*, 725. [Crossref]
56. Singh, G.; Kim, I. Y.; Lakhi, K. S.; Srivastava, P.; Naidu, R.; Vinu, A.; *Carbon* **2017**, *116*, 448. [Crossref]
57. Zhu, N.; Qian, F.; Xu, X.; Wang, M.; Teng, Q.; *Materials* **2021**, *14*, 6190. [Crossref]
58. Tischer, S.; Börnhorst, M.; Amsler, J.; Schoch, G.; Deutschmann, O.; *Phys. Chem. Chem. Phys.* **2019**, *21*, 16785. [Crossref]
59. Bai, J.; Huang, J.; Jiang, Q.; Jiang, W.; Demir, M.; Kilic, M.; Altay, B. N.; Wang, L.; Hu, X.; *Colloids Surf., A* **2023**, *674*, 131916. [Crossref]
60. Bai, J.; Huang, J.; Yu, Q.; Demi, M.; Akgul, E.; Altay, B. N.; Hu, X.; Wang, L.; *Front Chem. Sci. Eng.* **2023**, *17*, 1122. [Crossref]
61. Bai, J.; Shao, J.; Yu, Q.; Demir, M.; Altay, B. N.; Ali, T. M.; Jiang, Y.; F, L. W.; Hu, X.; *Chem. Eng. J.* **2024**, *479*, 147667. [Crossref]
62. Khuong, D. A.; Trinh, K. T.; Nakaoka, Y.; Tsubota, T.; Tashima, D.; Nguyen, H. N.; Tanaka, D.; *Chemosphere* **2022**, *299*, 134365. [Crossref]
63. Geng, J.-C.; Xue, D.-M.; Liu, X.-Q.; Shi, Y.-Q.; Sun, L.-B.; *AIChE J.* **2017**, *63*, 1648. [Crossref]
64. Wang, H.; Chen, C.; Chen, Y.; Wan, H.; Dong, L.; Guan, G.; *J. Environ. Chem. Eng.* **2021**, *9*, 105046. [Crossref]
65. Li, J.; Li, X.; Zhao, P.; Lei, D. Y.; Li, W.; Bai, J.; Ren, Z.; Xu, X.; *Carbon* **2015**, *84*, 460. [Crossref]
66. Kim, G.; Lee, J.; Liu, T.; Grey, C. P.; *J. Phys. Chem. C* **2021**, *125*, 10558. [Crossref]
67. Ferrari, A. C.; Robertson, J.; *Phys. Rev. B* **2000**, *61*, 14095. [Crossref]
68. Casiraghi, C.; Hartschuh, A.; Qian, H.; Piscanec, S.; Gerogi, C.; Fasoli, A.; Novoselov, K. S.; Basko, D. M.; Ferrari, A. C.; *Nano Lett.* **2009**, *9*, 1433. [Crossref]
69. Lee, S. M.; Lee, S. H.; Roh, J. S.; *Crystals* **2021**, *11*, 153. [Crossref]
70. Folomeshkin, M. S.; Pisarevsky, Y. V.; Prosekov, P. A.; Volkovsky, Y. A.; Kumskov, A. S.; Grigoriev, Y. V.; Ligacheva, E. A.; Targonskii, A. V.; Blagov, A. E.; Kovalchuk, M. V.; *Crystallogr. Rep.* **2019**, *64*, 1. [Crossref]

71. Sing, K. S. W.; Everett, D. H.; Haul, R. A. W.; Moscou, L.; Pierotti, R. A.; Rouquérol, J.; Siemieniewska, T.; *Pure Appl. Chem.* **1985**, *57*, 603. [Crossref]
72. Horvath, G.; Kawazoe, K.; *J. Chem. Eng. Jpn.* **1983**, *16*, 470. [Crossref]
73. Mckee, D. W.; *Carbon* **1982**, *20*, 59. [Crossref]
74. Nzihou, A.; Stanmore, B.; Sharrock, P.; *Energy* **2013**, *58*, 305. [Crossref]
75. Kim, M. J.; Choi, S. W.; Kim, H.; Mun, S.; Lee, K. B.; *Chem. Eng. J.* **2020**, *397*, 125404. [Crossref]
76. He, S.; Chen, G.; Xiao, H.; Shi, G.; Ruan, C.; Ma, Y.; Dai, H.; Yuan, B.; Chen, X.; Yang, X.; *J. Colloid Interface Sci.* **2021**, *582*, 90. [Crossref]
77. Li, H.; Tang, M.; Huang, X.; Wang, L.; Liu, Q.; Lu, S.; *Chem. Eng. J.* **2023**, *466*, 143095. [Crossref]
78. Wu, R.; Ye, Q.; Wu, K.; Wang, L.; Dai, H.; *J. CO₂ Util.* **2021**, *51*, 101620. [Crossref]
79. Gan, F.; Wang, B.; Guo, J.; He, J.; Ma, S.; Jiang, X.; Jin, Z.; *Sep. Purif. Technol.* **2022**, *302*, 122089. [Crossref]
80. Sevilla, M.; Fuertes, A. B.; *Energy Environ. Sci.* **2011**, *4*, 1765. [Crossref]
81. Vargas, D. P.; Giraldo, L.; Moreno-Piraján, J. C.; *Int. J. Mol. Sci.* **2012**, *13*, 8388. [Crossref]
82. Goel, C.; Kaur, H.; Bhunia, H.; Bajpai, P. K.; *J. CO₂ Util.* **2016**, *16*, 50. [Crossref]
83. Singh, V. K.; Anil Kumar, E.; *Appl. Therm. Eng.* **2016**, *97*, 77. [Crossref]
84. Shafeeyan, M. S.; Daud, W. M. A. W.; Shamiri, A.; Aghamohammadi, N.; *Energy Fuels* **2015**, *29*, 6565. [Crossref]
85. Chowdhury, S.; Balasubramanian, R.; *Ind. Eng. Chem. Res.* **2016**, *55*, 7906. [Crossref]
86. Musa, S. G.; Aljunid Merican, Z. M.; Haruna, A.; *J. Solid State Chem.* **2022**, *314*, 123363. [Crossref]
87. Patel, H. A.; Byun, J.; Yavuz, C. T.; *ChemSusChem* **2017**, *10*, 1303. [Crossref]
88. Yuan, X.; Li, S.; Jeon, S.; Deng, S.; Zhao, L.; Lee, K. B.; *J. Hazard Mater.* **2020**, *399*, 123010. [Crossref]
89. Chang, Q.; *Colloid and Interface Chemistry for Water Quality Control*; Elsevier, 2016, ch. 10. [Crossref]
90. Mukhtar, A.; Saqib, S.; Mellon, N. B.; Babar, M.; Rafiq, S.; Ullah, S.; Bustam, M. A.; Al-Sehemi, A. G.; Muhammad, N.; Chawla, M.; *J. Nat. Gas Sci. Eng.* **2020**, *77*, 103203. [Crossref]
91. Aghel, B.; Janati, S.; Wongwises, S.; Shadloo, M. S.; *Int. J. Greenhouse Gas Control* **2022**, *119*, 103715. [Crossref]

Submitted: December 14, 2023

Published online: March 18, 2024